pp 365–388. © The Author(s), 2020. Published by Cambridge University Press on behalf of Royal Aeronautical Society
doi:10.1017/aer.2020.63

Uncertainty analysis and robust shape optimisation for laminar flow aerofoils

J. Hollom and N. Qin
n.qin@sheffield.ac.uk
Department of Mechanical Engineering
The University of Sheffield
Sheffield
UK

ABSTRACT

Uncertainty in the critical amplification factor (N_{cr}) of the e^N transition model is used to approximate the uncertainty in the surface and flow quality of natural laminar flow (NLF) aerofoils. The uncertainty in N_{cr} is represented by a negative half-normal probability distribution that descends from the largest N_{cr} achievable with an ideal surface and flow quality. The uncertainty in various aerodynamic coefficients due to the uncertainty in N_{cr} is quantified using the weighted mean and standard deviation of flow solutions run at different N_{cr} values. The uncertainty in the aerofoil performance is assessed using this methodology. It is found that the standard deviation of the aerofoil performance due to the uncertainty in N_{cr} is largest when the transition location is most sensitive to changes in the lift coefficient at the ideal N_{cr}. Robust shape optimisation is also carried out to improve the mean performance and reduce the standard deviation of the performance with uncertainty in N_{cr}. This is found to be effective at producing aerofoils with a larger amount of laminar flow that are less sensitivity to uncertainty in N_{cr}. A trade-off is observed between the mean performance and the standard deviation of the performance. It is also found that reducing the standard deviation of the performance at one Mach number or lift coefficient design point can cause an increase in the standard deviation off-design.

Keywords: Laminar transition; Amplification Factor; Uncertainty Quantification; Robust Optimisation

NOMENCLATURE

$C(u)$	class function
$S(u)$	shape function
u	chord length position
A_R	class shape transformation coefficients

Received 25 September 2019; revised 10 June 2020; accepted 26 June 2020.

https://doi.org/10.1017/aer.2020.63 Published online by Cambridge University Press

n	Bernstein polynomial power
z_o/z_p	original/perturbed z coordinate
N_{cr}	critical N-factor
N_i	ideal critical N-factor
N_σ	standard deviation of critical N-factor
F	output variable function
$P(N_{cr})$	probability density function
W	summation of weights
k_r	number of N_{cr} samples
Tr_u	upper-surface transition location
Tr_l	lower-surface transition location

Greek symbol

$\Delta_{z_{te}}$	trailing-edge thickness
μ	mean
σ	standard deviation

1.0 INTRODUCTION

The passive extension of laminar flow over an aerodynamic surface, referred to as Natural Laminar Flow (NLF), is seen as a promising approach for the reduction of aircraft drag[1]. Obtaining NLF requires the suppression of boundary-layer instabilities, which are the cause of flow transition. This is achieved during NLF aerofoil design by tailoring the aerofoil's pressure distribution. However, the sensitivity of the transition location to the surface and flow quality makes effective implementation of NLF challenging. Early transition of the flow can occur for a number of reasons. These include contamination of the leading edge by insects, icing or debris[2,3], as well as in the presence of steps and gaps between panels or other irregularities in the surface finish and roughness[4,5].

Manufacturing aerodynamic surfaces without steps, gaps and other irregularities is difficult and costly. Methods for protecting the wing from contamination have also been proposed[6]. However, these are often complex and not able to guarantee contamination is avoided. An alternative to this is to obtain a NLF design that is insensitive to variations in the surface and flow quality. This is achieved using the robust design approach pioneered by Genichi Taguchi[7] that tries to improve the mean performance while reducing the standard deviation of the performance in the presence of uncertainty. To some degree, it can be considered an extension of multi-point design, which tries to improve the net performance at a range of conditions and has also been applied to the design of NLF aerofoils[8,9].

There has been extensive research on the robustness of fully turbulent aerofoils to uncertainty in the Mach and Reynolds numbers[10–19], but less applied to NLF design. Zhao et al.[20] carried out shape optimisation of a NLF aerofoil to improve the robustness of the maximum lift coefficient ($C_{l,\max}$) to uncertainty in the transition location. Zhao et al.[21] then carried out shape optimisation of a NLF aerofoil to improve the robustness of the drag to uncertainty in the Mach number. Jing et al.[22] also performed shape optimisation of an NLF aerofoil to improve the robustness of the drag to uncertainty in the Mach number and lift coefficient. While these studies consider the robustness of NLF performance to uncertainty in flight conditions or the transition location itself, research on the robustness of NLF aerofoils to

https://doi.org/10.1017/aer.2020.63 Published online by Cambridge University Press

uncertainty in the surface and flow quality has been limited. Salahudeen and Baeder[23] analysed the sensitivity of an aerofoil with a free transition to uncertainty in the flow quality by varying the free-stream turbulent intensity in the transport equation-based $\gamma - \mathrm{Re}_\theta$ transition model.

Modelling instability growth within the boundary layer is done using linear stability theory. The e^N transition model makes use of this by prescribing the transition at the point at which an instability wave first exceeds some critical amplification factor. This is typically referred to as the critical N-factor (N_{cr}). The transition occurs at a lower N_{cr} value, and so further upstream, if the surface or flow quality is reduced. It is therefore possible to approximate the effects of uncertainty in the surface and flow quality by applying uncertainty to the value of N_{cr} within the e^N transition model. Some work has been done using this relationship. Deng and Qiao[24] used an inverse design approach to obtain a NLF aerofoil with an N_{cr} envelope that sees little change in the transition location as N_{cr} is reduced. Han et al.[25] optimised a NLF wing using N_{cr} values lower than expected to account for the uncertainty in real flight conditions. Rashad and Zingg[9] analysed this approach and found that optimising for a reduced N_{cr} was no guarantee of performance at higher N_{cr}, given that extended laminar flow can increase the risk of flow separation. They then carried out multi-point optimisation over three N_{cr} values to ensure that aerofoil performance was maintained at off-design conditions.

There are two main objectives to this study. The first is to investigate the sensitivity of aerofoil performance to uncertainty in N_{cr}. The second objective is to carry out robust shape optimisation with the goal of improving the robustness of aerofoils to uncertainty in N_{cr}. In both cases, uncertainty in N_{cr} is used to qualitatively account for the uncertainty in the surface and flow variability. While direct modelling of surface and flow quality effects on the transition lies beyond the scope of this study, it is assumed that these unknowns may be crudely incorporated through a reduced N_{cr} criterion.

2.0 ANALYSIS METHODOLOGY

2.1 Uncertainty distribution

The uncertainty in N_{cr} is modelled using a probability distribution, which is assumed to take a form similar to the uncertainty that would be seen in the surface and flow quality. As there is little information available on this in literature, a distribution with a heuristic form is used. The heuristic form is selected using an intuitive assessment of the uncertainty in the free-stream turbulence, surface finish, wear and contamination.

The free-stream turbulence is an environmental condition, so its uncertainty would best be described using a normal probability distribution. Machining inaccuracy is more likely to produce surface imperfections than a better-than-expected finish, and surface wear and contamination only act to degrade the surface quality further. A negative half-normal probability distribution would therefore be suitable for describing the uncertainty in each. As the free-stream turbulence is low during flight, surface finish, wear and contamination are assumed to be the dominant sources of uncertainty. Therefore, a negative half-normal probability distribution is used during this study as a heuristic representation of the uncertainty in N_{cr}. Figure 1 shows three example negative half-normal N_{cr} probability distributions. Each has the same ideal N_{cr} (N_i) but different standard deviations of N_{cr} (N_σ). The negative half-normal distribution is represented by the probability density function $P(N_{cr})$ shown in Equation (1).

$$P(N_{cr}) = \frac{\sqrt{2}}{N_\sigma \sqrt{\pi}} \exp\left(-\frac{(N_{cr} - N_i)^2}{2N_\sigma^2}\right); \quad N_{cr} \leq N_i \qquad \ldots (1)$$

https://doi.org/10.1017/aer.2020.63 Published online by Cambridge University Press

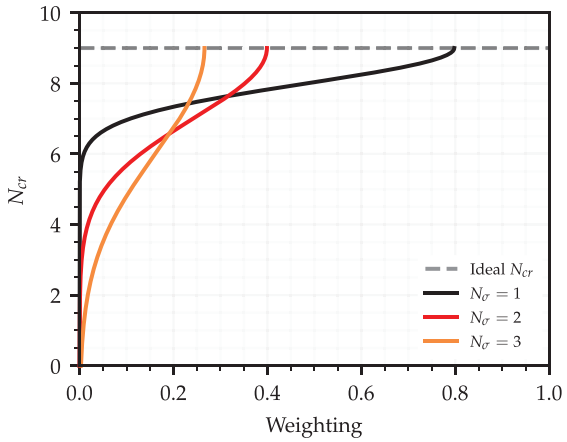


Figure 1. Examples of negative half-normal N_{cr} probability distributions with the same ideal N_{cr} but different standard deviations in N_{cr} (N_σ).

It should be noted that it may not always be appropriate to ignore the probability of N_{cr} increasing. Rashad and Zingg[9] found that operating an aerofoil at a higher N_{cr} than it was designed for could result in laminar separation of the flow and a significant drop in performance. Thus, a skewed distribution may be more appropriate if the probability of $N_{cr} > N_i$ is significant. However, as the intuitive analysis of the uncertainty sources carried out by those authors suggests that the probability of $N_{cr} > N_i$ is very low, this has not been used for this study.

2.2 Uncertainty propagation and quantification

A sampling-based approach has been used to propagate the uncertainty in N_{cr} through the aerodynamic model. Aerofoil designs are evaluated with different N_{cr} values sampled at regular intervals over the range of possible values. The results of each evaluation are weighted by the probability of that N_{cr} value occurring. The uncertainty in the results is then quantified by taking the standard deviation of these weighted values.

The standard deviation F_σ of an output variable $F(N_{cr})$ is calculated using Equation (2), where k_r is the number of N_{cr} samples used, F_μ is the weighted mean of the output variable $F(N_{cr})$ calculated using Equation (3) and W is the sum of the probability weights found using Equation (4). $P(N_{cr})$ is the probability weighting calculated using Equation (1). The term F_σ is therefore a measure of how much some output variable $F(N_{cr})$ varies with uncertainty in N_{cr}. Reducing F_σ thus improves the robustness of the output variable to this uncertainty.

$$F_\sigma = \sqrt{\frac{1}{W}\sum_{j=1}^{k_r}\left[F(N_{cr_j}) - F_\mu\right]^2} \quad \ldots(2)$$

$$F_\mu = \frac{1}{W}\sum_{j=1}^{k_r} P(N_{cr_j})F(N_{cr_j}) \quad \ldots(3)$$

https://doi.org/10.1017/aer.2020.63 Published online by Cambridge University Press

$$W = \sum_{j=1}^{k_r} P(N_{cr_j}) \quad \ldots (4)$$

The benefit of using uniformly distributed weighted samples over a random sampling method such as Monte Carlo is that far fewer sample points are needed. This is because the evenly spaced samples have perfect equidistribution. This reduces the computational cost, as each sample point represents a model evaluation. The spacing between N_{cr} sample points determines the accuracy of the mean and standard deviation values calculated.

However, given the periodic nature of this sampling strategy, it is unsuitable for models exhibiting oscillatory behaviour at a frequency close to that of the samples. In most cases, this will not be an issue as the transition location on both the upper and lower aerofoil surfaces will move monotonically upstream as N_{cr} is reduced. However, some oscillations in transition location may be seen as N_{cr} is reduced if laminar separation is present. In these cases, the transition location would move upstream of the separation point as N_{cr} is reduced. The separation point may then move downstream as turbulent flow can more easily resist flow separation. The resulting lift increase would allow for the same lift coefficient to be maintained at a lower incidence angle. This would in turn result in a more positive pressure gradient on the upper surface, which helps to suppress instability growth and so will move the transition location downstream. In these cases, the accuracy of the uncertainty quantification carried out may be low if an insufficient number of N_{cr} samples are used.

2.3 Computational solvers

Two efficient flow solvers were used during this study. The first, used for analysis and optimisation at subsonic conditions, was XFOIL, developed by Drela[26]. This is a 2D flow analysis tool which uses the viscous–inviscid interaction (VII) approach to couple a potential flow panel method with an integral boundary-layer solution and a simplified incompressible e^N transition model[27]. Additional corrections are included to account for weak compressibility effects and mild separation. Simulations were run with 300 panels during this study, which is near the maximum allowed by XFOIL. This was done to ensure that the results were independent of the number of panels used. While XFOIL is considered to be a low-fidelity solver given its use of VII over the Reynolds-averaged Navier–Stokes approach, it is a highly reliable tool when operated within its limitations and has been used extensively in industry.

For analysis and optimisation at transonic conditions, the CVGK flow solver[28] was used. This is derived from BVGK, which was developed by the ex-Royal Aircraft Establishment. CVGK also uses a VII approach[29], modelling inviscid flow using the Garabedian and Korn[30] (G&K) full potential flow method (with additional improvements as outlined by Lock[31]) and viscous flow using the lag-entrainment integral method[32]. This has been coupled with an e^N transition model[33] capable of both incompressible and compressible stability analyses. The compressible e^N method is used throughout this work. CVGK is able to model un-swept, infinity swept and swept–tapered wings. As such, it allows for the specification of both Tollmien–Schlichting and crossflow instability N_{cr} values. CVGK has been extensively used for transonic wing design in the UK aerospace industry and validated at swept and un-swept transonic flow conditions[28,34]. Atkin and Gowree[28] found good agreement between computational results from CVGK and wind-tunnel results for the RAE5237 and RAE5240 from $0.6 < M < 0.85$. It was, however, found that CVGK slightly under-estimated the shock strength at high Mach numbers. CVGK was found to produce mesh-independent results over

https://doi.org/10.1017/aer.2020.63 Published online by Cambridge University Press

the Mach range investigated with 240 cells in the stream-wise direction and 48 in the wall-normal direction. To increase the transition location accuracy during this study, 320 cells were used in the stream-wise direction for all simulations.

3.0 CRITICAL N-FACTOR UNCERTAINTY ANALYSIS

3.1 Definition of subsonic problem

The NLF0215 aerofoil[35] has been analysed using the proposed methodology to investigate how its performance varies with uncertainty in N_{cr}. This is a flapped aerofoil developed for low drag at a cruise lift coefficient of $C_l = 0.2$ and climb lift coefficient range of $0.5 < C_l < 1.0$. The design Reynolds number and Mach number were $\mathrm{Re} = 9 \times 10^6$ and $\mathrm{M} = 0.1$. A fixed flap deflection angle of 0° is used during this study. Analysis of the aerofoil is carried out at the cruise Reynolds number of $\mathrm{Re} = 9 \times 10^6$ and Mach number of $\mathrm{M} = 0.1$ over the lift coefficient range of $0 \leq C_l \leq 1.6$ with the angle-of-attack left free. Practical implementation of NLF will require some form of protection from leading-edge contamination[36]. It is assumed that a method such as liquid discharge[6] can be used for subsonic applications. This approach protects both the upper and lower surfaces from contamination, so the transition is left free on both during this study.

The probability distribution describing the uncertainty in N_{cr} has an ideal value of $N_i = 9$ and a standard deviation of $N_\sigma = 2$. $N_i = 9$ is selected as the simplified e^N model in XFOIL is based on the e^9 method of Smith and Gamberoni[37]. This value is also used in other studies on aerofoil performance at similar flow conditions[38,39,9]. The value of N_σ is selected somewhat arbitrarily, and so the effect of varying N_σ is also included in the analysis. The mean performance and standard deviation of the performance of the aerofoil are calculated at each lift coefficient. This is done using flow solutions evaluated with N_{cr} values taken in steps of 0.1 from $N_{cr} = 9 \rightarrow 0$.

3.2 Subsonic analysis

Figure 2 shows the drag and transition polars of the NLF0215 when $N_{cr} = 9$. The drag polar includes the total drag (C_d) with the skin friction (C_{df}) and pressure drag (C_{dp}) components. The transition polar includes the upper-surface (Tr_u) and lower-surface (Tr_l) transition locations. Figure 3 shows the standard deviation of the drag components and transition locations with uncertainty in N_{cr}. The standard deviation of each variable is represented by the subscript σ.

The total drag polar exhibits a bucket shape between $0.5 < C_l < 1.0$. This is a common feature of NLF aerofoil designs, where laminar flow is extended on both surfaces through the design lift coefficient range but is quickly lost when moving off-design. Tr_σ is largest on each surface where the transition location is most sensitive to the lift coefficient. As the peaks in $Tr_{u|\sigma}$ and $Tr_{l|\sigma}$ overlap, $C_{d|\sigma}$ is high through the entire drag bucket lift coefficient range. Although the peak in Tr_σ for the upper surface is smaller, the corresponding peak in $C_{d|\sigma}$ is larger. This is because a change in the upper-surface transition location has a stronger effect on the lift coefficient. As the angle-of-attack is varied to obtain the desired lift coefficient, this causes both the skin friction and pressure drag to vary. The standard deviation of C_d is larger as a result. The sensitivity of the pressure drag to the lift coefficient is larger at higher lift coefficients. This is apparent in the $C_{d|\sigma}$ polar, where the standard deviation of C_{dp} is large at high lift coefficients while Tr_σ is low for both surfaces. The $C_{d|\sigma}$ polar therefore takes the

https://doi.org/10.1017/aer.2020.63 Published online by Cambridge University Press

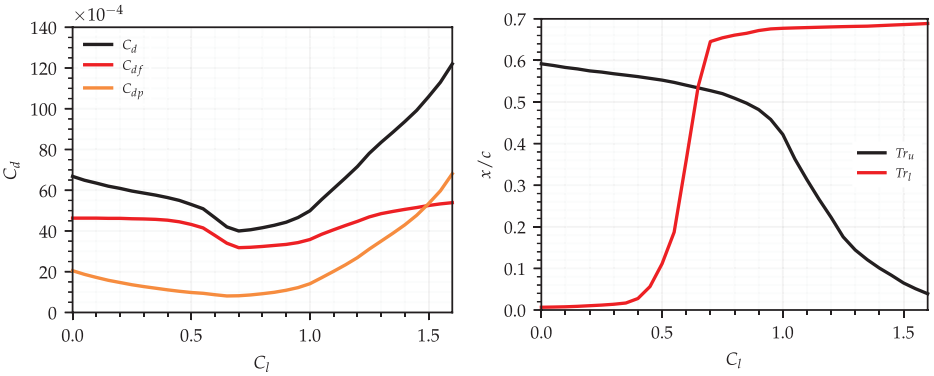


Figure 2. Drag and transition location polars for the NLF0215 when $N_{cr} = 9$.

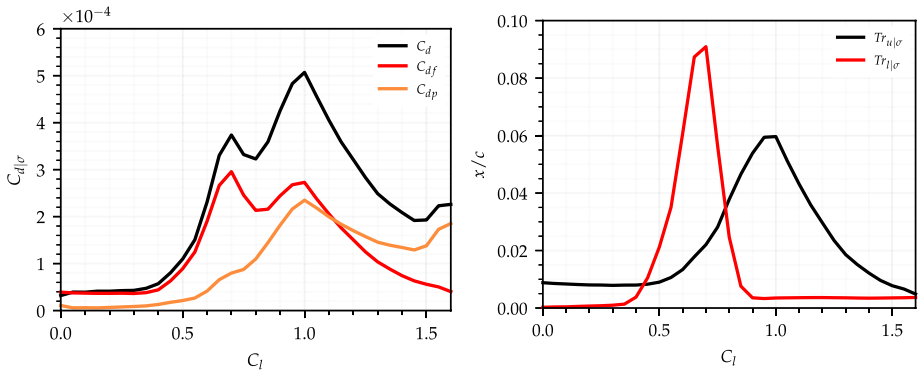


Figure 3. Standard deviation of drag and and transition location polars for the NLF0215.

shape of the combined Tr_σ polars at low lift coefficient values, but diverges from this as the lift coefficient is increased.

Figure 4 shows the pressure distributions and N-factor envelopes for the NLF0215 at lift coefficients of $C_l = 0.4$, $C_l = 0.7$ and $C_l = 1.0$ when $N_{cr} = 9$. These help to explain why Tr_σ is largest on each surface when the transition location at the ideal N_{cr} is most sensitive to changes in the lift coefficient. A strong adverse pressure gradient on both surfaces at $C_l = 0.4$ precedes transition. Varying the lift coefficient has little effect on the transition location, as the strength and direction of the pressure gradient are largely unaffected. The lower-surface transition is close to the leading edge and so also insensitive to N_{cr}. The upper-surface transition follows a long favourable pressure gradient that suppresses instability growth until rapid growth occurs just upstream of the transition point. Transition is therefore insensitive to reductions in N_{cr} until N_{cr} is reduced significantly. A weak pressure gradient precedes the transition on the lower surface at $C_l = 0.7$ and on the upper surface at $C_l = 1.0$. Varying the lift coefficient now has a large effect on the transition location, as the direction of the pressure gradient can change over a large chord length. The weak pressure gradient also promotes gradual instability growth up to the transition location. Therefore, only a small reduction in N_{cr} is needed to shift the transition upstream.

https://doi.org/10.1017/aer.2020.63 Published online by Cambridge University Press

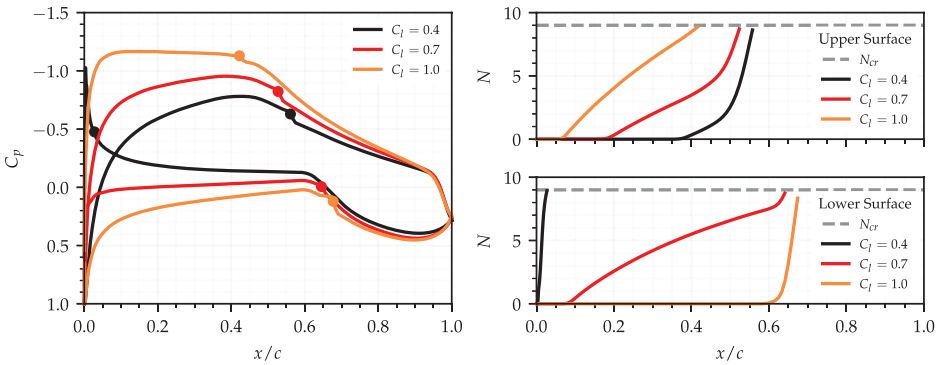


Figure 4. Pressure distributions and N-factor envelopes for the NLF0215 at $C_l = 0.4$, 0.7 and 1.0 with $N_{cr} = 9$. Markers on the pressure distributions indicate transition locations.

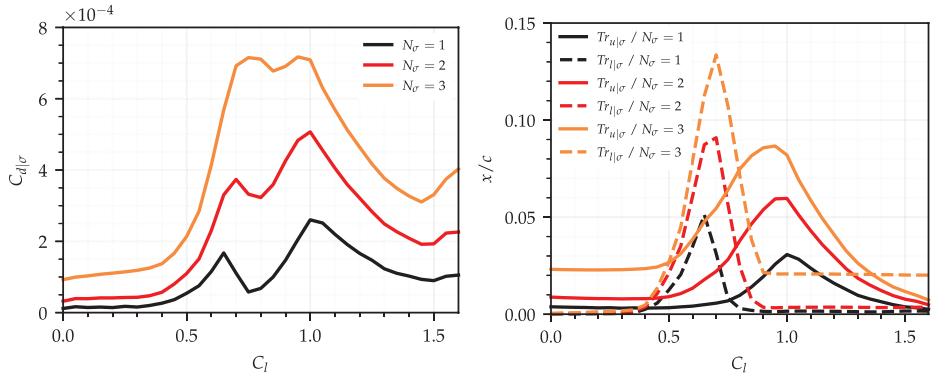


Figure 5. Standard deviation of drag and transition location polars for the NLF0215 when calculated with different standard deviations of N_{cr}.

The shape of the $C_{d|\sigma}$ and Tr_σ polars can therefore be inferred from the drag and transition polars found at the ideal N_{cr}. Tr_σ is found to be directly related to the rate of change of the transition location with the lift coefficient at the ideal N_{cr}, and $C_{d|\sigma}$ is proportional to the sum of the upper- and lower-surface Tr_σ. It is important to note that this may not hold if a different N_{cr} uncertainty distribution or standard deviation of N_{cr} is selected. The uncertainty distribution chosen gives the highest probability weighting to the ideal N_{cr}. Therefore, the sensitivity of the transition locations to changes in the lift coefficient at the ideal N_{cr} has the greatest effect on Tr_σ. This relationship will diminish if the probability weighting at the ideal N_{cr} is reduced. Figure 5 shows the standard deviation of C_d and the standard deviation of Tr polars when calculated with different standard deviations of N_{cr} (N_σ).

The value of $C_{d|\sigma}$ and Tr_σ grows at all lift coefficients as N_σ is raised. The increase in Tr_σ is greatest for each surface where Tr_σ is already large. However, Tr_σ increases everywhere where extended laminar flow is achieved at the ideal N_{cr}. Regardless of the N_σ value chosen, the $C_{d|\sigma}$ polar still has the same form as the combined Tr_σ polars at low lift coefficient values. However, the $C_{d|\sigma}$ polar deviates more from this at higher lift coefficients if N_σ is larger.

https://doi.org/10.1017/aer.2020.63 Published online by Cambridge University Press

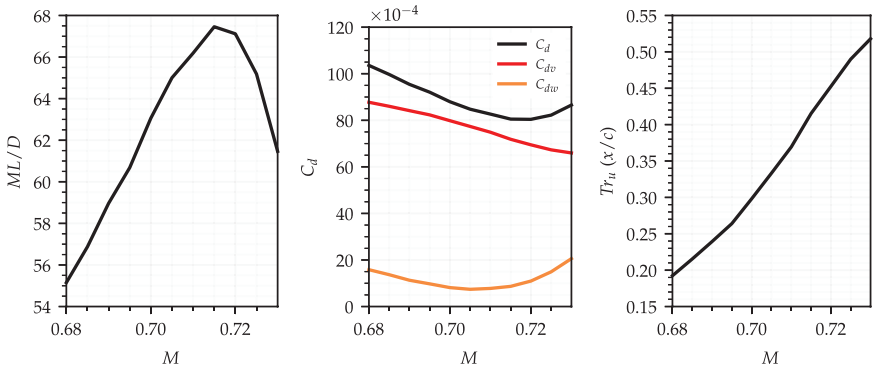


Figure 6. ML/D, drag and upper-surface transition location polars for the RAE2822 when $N_{cr} = 9$.

3.3 Definition of transonic problem

The RAE2822 aerofoil[40] has also been analysed using the proposed methodology to investigate how its performance varies with uncertainty in N_{cr}. This is a supercritical aerofoil designed for $C_l = 0.56$ at $\mathrm{M} = 0.66$ with the transition fixed near the leading edge on both surfaces. During this study, the transition remains fixed on the lower surface at $0.03x/c$ but is free to move on the upper surface. A popular method for fixing the transition on the lower surface to protect the leading edge from contamination on large transonic aircraft is the use of a Krueger flap[41–43]. This shields the leading edge when deployed during take-off, before being retracted into the lower surface during cruise. This leaves the upper surface free of contamination but triggers an early transition on the lower surface. Initial analysis of the aerofoil at a Reynolds number of $\mathrm{Re} = 6.5 \times 10^6$ and $N_{cr} = 9$ with a free transition on the upper surface found that $(ML/D)_{\max}$ occurs at approximately $\mathrm{M} = 0.715$ and $C_l = 0.76$. This is used to fix $\mathrm{M}^2 C_l$ while varying the Mach number between $0.68 < \mathrm{M} < 0.73$. The angle-of-attack is varied to obtain the target lift coefficient at each Mach number.

The probability distribution describing the uncertainty in N_{cr} again has an ideal value of $N_i = 9$ and a standard deviation of $N_\sigma = 2$. $N_i = 9$ is selected as it lies between the values of N_{cr} obtained from the compressible e^N stability analysis of ATTAS and FOKKER 100 NLF flight test data without the presence of crossflow instability growth[44,45]. $N_\sigma = 2$ is again selected somewhat arbitrarily, with the effect of varying N_σ included in the analysis. The mean performance and the standard deviation in the performance of the aerofoil are calculated at each Mach number–lift coefficient combination. This is again done using flow solutions evaluated with N_{cr} values taken at steps of 0.1 from $N_{cr} = 9 \to 0$.

3.4 Transonic analysis

Figure 6 shows the ML/D, drag (C_d) and upper-surface transition location (Tr_u) polars for the RAE2822 when $N_{cr} = 9$. The drag polar is broken down into viscous (C_{dv}) and wave drag (C_{dw}) components. Figure 7 shows the standard deviation of each with uncertainty in N_{cr}. The standard deviation is denoted by the subscript σ.

The total drag is dominated by the viscous drag component at the ideal N_{cr} for the considered Mach number range. As $\mathrm{M}^2 C_l$ is fixed, increasing the Mach number reduces the lift coefficient and the angle-of-attack. This leads to a near-linear reduction in the viscous drag as the transition location moves downstream. The maximum ML/D coincides with the minimum drag. This occurs at the point where increasing the Mach number causes a rise in the wave

https://doi.org/10.1017/aer.2020.63 Published online by Cambridge University Press

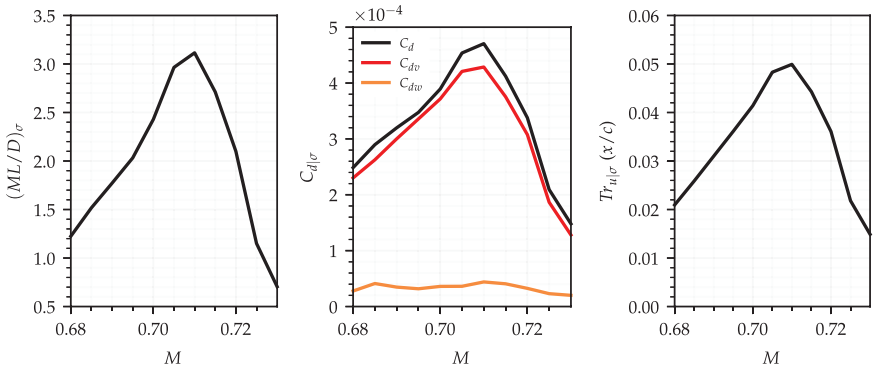


Figure 7. Standard deviation of ML/D, drag and upper-surface transition location polars for the RAE2822.

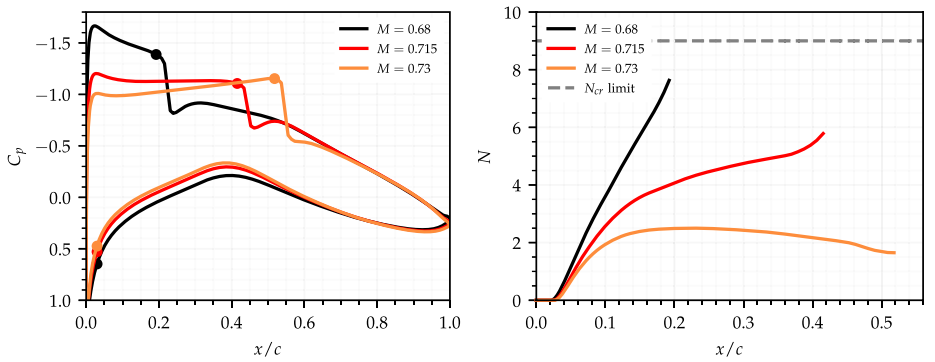


Figure 8. Pressure distributions and N-factor envelopes for the RAE2822 at M = 0.680, 0.715 and 0.730 with $N_{cr} = 9$. Markers on the pressure distributions indicate transition locations.

drag that outweighs the reduction in the viscous drag. $(ML/D)_\sigma$ and $C_{d|\sigma}$ are both largest at a Mach number just below this. As the total drag is dominated by the viscous drag component, the $C_{d|\sigma}$ and $Tr_{u|\sigma}$ polars are very similar.

The shape of the $Tr_{u|\sigma}$ polar can be explained using Fig. 8 showing the pressure distributions and N-factor envelopes for the RAE2822 at Mach numbers of M = 0.680, M = 0.715 and M = 0.730 when $N_{cr} = 9$. A strong favourable pressure gradient is obtained at the lower end of the Mach number range where the lift coefficient is small. This suppresses instability growth and delays the transition up to the shock position. As instability growth is suppressed, the transition location only moves upstream once N_{cr} is significantly reduced. $Tr_{u|\sigma}$ is therefore small. A strong adverse pressure gradient is obtained at the upper end of the Mach number range where the lift coefficient is large. Although this causes upstream instability growth, the transition at the ideal N_{cr} occurs closer to the leading edge, so reducing N_{cr} can only lead to a small reduction in laminar flow. $Tr_{u|\sigma}$ is therefore small. In both cases, Tr_σ is small when the transition is shock induced at the ideal N_{cr}, as reducing N_{cr} has no initial effect on the transition location. All three N-factor envelopes shown end at the point of shock-induced transition and so fail to reach $N_{cr} = 9$.

https://doi.org/10.1017/aer.2020.63 Published online by Cambridge University Press

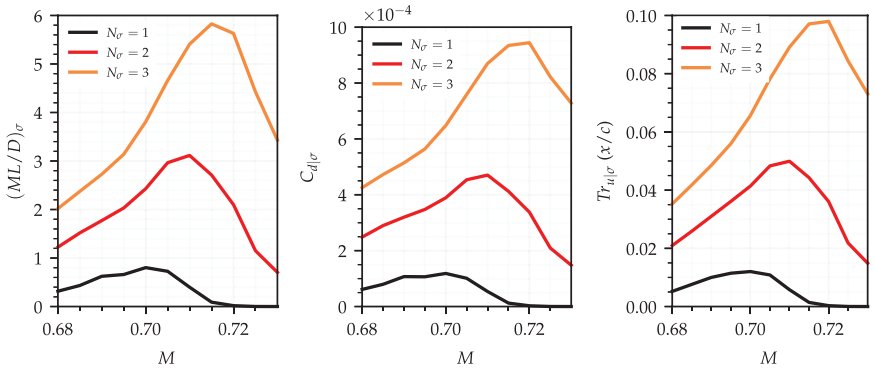


Figure 9. Standard deviation of ML/D, drag and upper-surface transition location polars for the RAE2822 when calculated with different standard deviations of N_{cr} uncertainty.

The effect that the standard deviation of N_{cr} uncertainty has on the aerofoil performance is again assessed. Figure 9 shows the $(ML/D)_\sigma$, $C_{d|\sigma}$ and $Tr_{u|\sigma}$ polars when calculated with different standard deviations of N_{cr} uncertainty. As expected, all three standard deviation polars grow in magnitude as N_σ is increased. The increase is comparable between the polars and largest at higher Mach numbers, as this is where there is the largest amount of laminar flow at the ideal N_{cr}. If there is a larger amount of laminar flow at the ideal N_{cr}, a larger amount is lost as N_{cr} is reduced from the ideal value to zero. If there is strong instability suppression, this shift in the transition location will occur at small N_{cr} values with low probability and have little effect on Tr_σ. However, the probability only needs to increase slightly for this loss of laminar flow to have a much larger effect on the calculated Tr_σ.

4.0 ROBUST OPTIMISATION

4.1 Problem formulation

Two multi-objective shape optimisation cases have been considered. The goal of each was to improve the aerofoil performance with uncertainty in N_{cr}. The NLF0215 aerofoil with a fixed flap deflection angle of 0° is used as a starting shape for a subsonic optimisation case. This is optimised at a Reynolds number of $\mathrm{Re} = 9 \times 10^6$, Mach number of $\mathrm{M} = 0.1$ and lift coefficient of $C_l = 0.7$. The optimisation objectives used are minimisation of the mean drag and the standard deviation of the drag with uncertainty in N_{cr}. The angle-of-attack is left free for the flow solver to control so that the target lift coefficient can be obtained. The transition is left free on both surfaces.

The RAE2822 aerofoil is used as the starting shape for a transonic optimisation case. This is optimised at a Reynolds number of $\mathrm{Re} = 6.5 \times 10^6$, Mach number of $\mathrm{M} = 0.715$ and lift coefficient of $C_l = 0.76$. The optimisation objectives used are maximisation of the mean ML/D and minimisation of the standard deviation of ML/D with uncertainty in N_{cr}. The angle-of-attack is again left free for the flow solver to control. The transition is left free on the upper surface but is fixed at $0.03x/c$ on the lower surface.

The mean performance and the standard deviation of the performance are calculated using the proposed uncertainty quantification method in both cases. The probability distribution describing the uncertainty in N_{cr} has an ideal value of $N_i = 9$ and a standard deviation of

https://doi.org/10.1017/aer.2020.63 Published online by Cambridge University Press

$N_\sigma = 2$, matching the values used during the uncertainty analysis. The optimiser changes the aerofoil shape using 6 design variables per surface for a total of 12. These come from the selected parameterisation method discussed in detail below. Bounds are placed on each design variable so that the optimiser has a finite design space to explore. The selection of these are also outlined below. Both cases have a constraint placed on the maximum aerofoil thickness, ensuring that all the optimised designs have a maximum thickness that is larger than or equal to that of the starting aerofoil.

A Python-based genetic algorithm is used to conduct the optimisation. This is implemented using the Distributed Evolutionary Algorithms in Python (DEAP) package[46] and interfaces with the external flow solver used in each case. Genetic algorithms replicate the selection, mating and mutation processes found in natural evolution, creating successive generations of new designs that combine the favourable characteristics of their predecessors. Initial designs are generated randomly within the design variable bounds and checked against the geometric constraints before being evaluated. Designs from this initial generation are selected using the NSGA-2 non-dominated method[47], mated using simulated binary crossover[48] and mutated using the bound polynomial mutation method[49]. New designs obtained through this process are then evaluated. This is repeated until a limit on the number of generations to evaluate is reached.

4.2 Parameterisation

There are various approaches to aerofoil parameterisation that can be grouped into two distinct categories: constructive and deformative[50]. Constructive methods define the aerofoil shape itself, while deformative methods define a perturbation profile which is then used to deform a starting aerofoil shape. A deformation approach is used in this study as it allows for optimisation of a complex starting aerofoil using a small number of design variables. When using a genetic algorithm, the number of designs needed per generation is between two and ten times the number of design variables used[51,52]. It is, therefore, desirable to use a small number of design variables.

New aerofoil shapes are obtained by changing the z coordinate of a starting aerofoil by some amount defined using a perturbation profile. This is represented mathematically in Equation (5), where z_o is the original aerofoil z coordinate and z_p is the perturbation z coordinate. u is the chord length position x/c.

$$z(u) = z_o(u) + z_p(u) \quad \ldots (5)$$

The perturbation profile is parameterised using the Class Shape Transformation (CST) method developed by Kulfan[53]. This is shown in Equation (6), where $\Delta_{z_{te}}$ is the trailing-edge thickness while $C(u)$ and $S(u)$ are the class and shape functions from the CST method.

$$z_p(u) = C(u)\, S(u) + \left(u\, \Delta_{z_{te}}\right) \quad \ldots (6)$$

The class function is defined in Equation (7), where n_1 and n_2 are exponents that determine the basic shape of the CST fitting. The values $n_1 = 0.5$ and $n_2 = 1.0$ are used to define a round-nosed aerofoil with finite trailing-edge gradient as the CST is commonly used for constructive aerofoil parameterisation. Values of $n_1 = n_2 = 1$ are used for this application.

$$C(u) = u^{n_1}\, (1-u)^{n_2} \quad \ldots (7)$$

https://doi.org/10.1017/aer.2020.63 Published online by Cambridge University Press

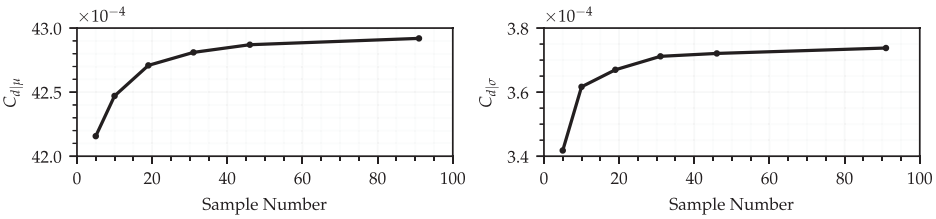


Figure 10. Mean and standard deviation of drag calculated with a varying number of N_{cr} samples for the NLF0215 aerofoil at $C_l = 0.7$, M = 0.1 and Re = 9×10^6.

The shape function given in Equation (8) contains n number of CST coefficients, A_r. These are the design variables controlled by the optimiser. As the optimiser varies each of these coefficients, the magnitude of the perturbation profile will change, deforming the original aerofoil and so creating new aerofoil designs. In both the subsonic and transition optimisation cases, six CST coefficients are used to define the perturbation profile on each surface. Therefore, the optimiser is in control of 6 design variables per surface, or 12 design variables in total.

$$S(u) = \sum_{r=0}^{n} A_r \frac{n!}{r!(n-r)!} u^r (1-u)^{n-r} \quad \ldots (8)$$

Upper and lower bounds were placed on the design variables during optimisation. In both cases, these were selected to allow for a large design space to be explored while also attempting to prevent the generation of infeasible designs, which would waste computational resources and slow down the progress of the optimiser.

4.3 Uncertainty sampling

The number of N_{cr} sample points used should be as small as possible while still being sufficient to calculate the mean performance and the standard deviation of the performance of an aerofoil with acceptable accuracy. This is because each sample point requires a flow solution, and so additional sample points increase the computational cost substantially. To determine the minimum number of sample points needed, a sample dependence study has been carried out for both the NLF0215 and RAE2822 aerofoils at the flow conditions to be used during their optimisation. For each aerofoil, a number of N_{cr} samples are taken at regular intervals between the ideal $N_{cr} = 9$ and $N_{cr} = 0$. The performance of the aerofoil is calculated at the design Mach number, Reynolds number and lift coefficient with each of the N_{cr} values. These are then weighted by the probability of that N_{cr} value occurring and used to calculate the mean and standard deviation of the performance with uncertainty in N_{cr}. This process is repeated for different numbers of N_{cr} samples. The mean and standard deviation of the aerofoil performance can then be plotted against the number of N_{cr} samples used, to assess the accuracy obtained as the number of samples is varied.

Figure 10 shows the mean drag and the standard deviation of the drag for the NLF0215 when calculated with different numbers of N_{cr} samples. Figure 11 shows the mean ML/D and the standard deviation of ML/D for the RAE2822 when calculated with different numbers of N_{cr} samples. As expected, the mean and standard deviation converge as the number of samples used increases for both cases. The mean drag is within 0.4% and the standard deviation of the drag is within 2% of the values found using 91 samples when only 19 samples are used for the NLF0215. The mean ML/D is within 0.003% and the standard deviation of ML/D is

https://doi.org/10.1017/aer.2020.63 Published online by Cambridge University Press

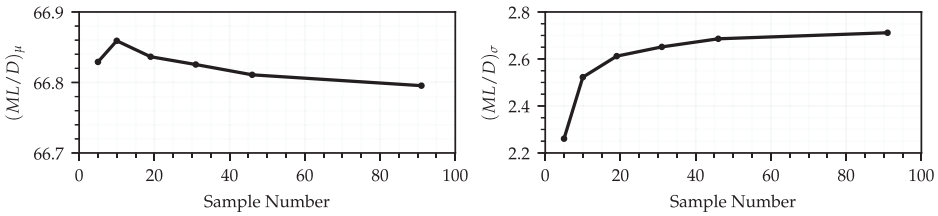


Figure 11. Mean ML/D and standard deviation of ML/D calculated with a varying number of N_{cr} samples for the RAE2822 aerofoil at $C_l = 0.76$, $M = 0.715$ and $Re = 6.5 \times 10^6$.

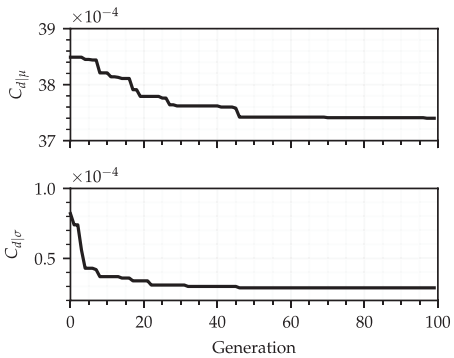


Figure 12. Minimum mean drag and standard deviation of drag found during the optimisation.

within 3% of the values found using 91 samples when only 19 sample points are used for the RAE2822. Thus, it is felt that 19 N_{cr} samples taken at intervals of 0.5 over the N_{cr} range gives acceptable accuracy while reducing the computational cost as much as possible.

5.0 RESULTS

5.1 Subsonic results

The optimisation produced 4,800 unique designs before the 100 generations limit. XFOIL was able to converge 3,051 of these at all N_{cr} sample points. Figure 12 shows the minimum mean drag ($C_{d|\mu}$) and the standard deviation of the drag ($C_{d|\sigma}$) found during the optimisation. After approximately 50 generations, the value of each is close to the final value found. Further iterations therefore primarily serve to explore the trade-off between objectives. Figure 13 shows designs on the Pareto front found between the two objective functions. All designs are at least 2 mean drag counts lower than the NLF0215 at the chosen design conditions and have a 3 drag count or more decrease in the standard deviation of the drag. The optimised aerofoils with the smallest $C_{d|\mu}$ and $C_{d|\sigma}$ are also indicated on the Pareto front. These are selected for comparison against the NLF0215, and are denoted as design M (standing for minimum mean drag) and design S (standing for minimum standard deviation of drag).

Figure 14 shows aerofoil profiles for the NLF0215 and selected optimised designs. The grey-shaded area indicates the viable design region as dictated by the design variable bounds. Both optimised aerofoils have common NLF design characteristics such as an increased maximum thickness located further aft and an increased curvature at the leading edge of the upper

https://doi.org/10.1017/aer.2020.63 Published online by Cambridge University Press

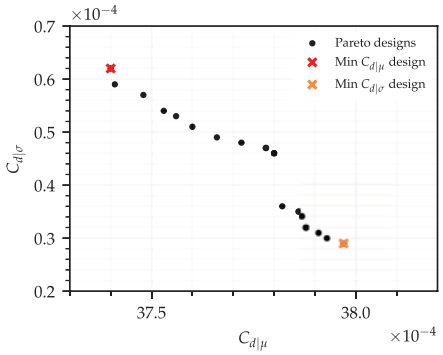


Figure 13. Mean drag and standard deviation of drag for Pareto-front aerofoil designs.

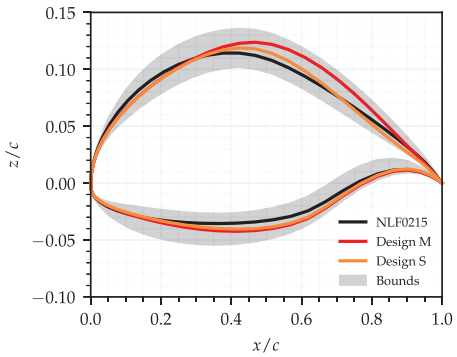


Figure 14. Aerofoil profiles for the NLF0215 and selected optimised designs.

surface followed by a reduced curvature between $0.05 < x/c < 0.4$. In combination, this creates a more favourable pressure gradient which thus delays the transition. This can be seen in Fig. 15, which shows the pressure distributions for the NLF0215 and selected optimised designs at the ideal N_{cr} of $N_{cr} = 9$. Some differences are seen between the two optimised designs despite their similar $C_{d|\mu}$ and $C_{d|\sigma}$ values. Design M is thicker than design S towards the rear of the aerofoil and so requires a smaller angle-of-attack to generate the same lift. This results in a longer upper-surface favourable pressure gradient and so more laminar flow. The smaller angle-of-attack has little effect on the lower-surface pressure gradient.

Figure 16 shows the drag and transition locations with varying N_{cr} for the NLF0215 and selected optimised designs. These were obtained using N_{cr} samples taken at intervals of 0.1 as done during the uncertainty analysis carried out previously. As expected, both optimised designs have lower drag than the NLF0215 over almost all of the N_{cr} range. The reduction in drag is small at the ideal N_{cr} but becomes much greater as N_{cr} is reduced. While both optimised designs have only a slightly delayed transition at the ideal N_{cr} on each surface, this is maintained down to much smaller N_{cr} values.

To delay the transition at the ideal N_{cr}, the favourable pressure gradient up to the transition location should be as long as possible. However, its strength must be weak to avoid flow separation caused by the strong adverse pressure that will inevitably follow it. A weak favourable

https://doi.org/10.1017/aer.2020.63 Published online by Cambridge University Press

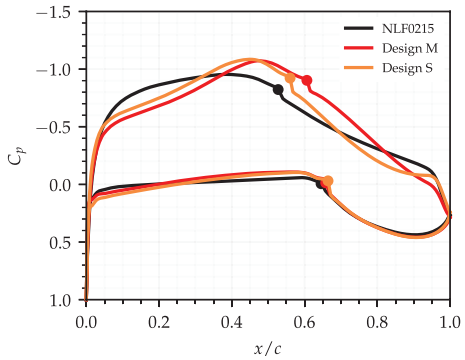


Figure 15. Pressure distributions for the NLF0215 and selected optimised designs at $N_{cr} = 9$. Markers indicate transition location.

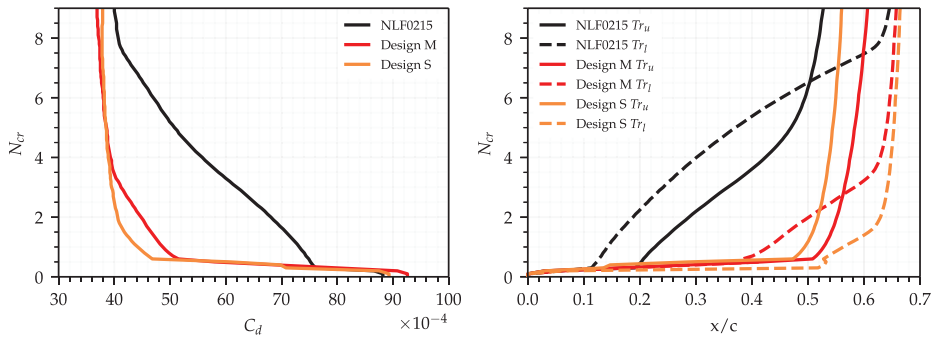


Figure 16. Variation of drag and transition locations with changes in N_{cr} for the NLF0215 and selected optimised designs.

pressure gradient will delay the transition at the ideal N_{cr} but see stronger upstream instability growth. It will therefore be more sensitive to the lift coefficient and N_{cr}. A shorter but stronger favourable pressure gradient has the inverse effect. This can be seen in the differences between designs M and S. A more favourable pressure gradient up to the location of minimum pressure helps design S keep Tr_l extended down to lower N_{cr} values. A stronger adverse pressure gradient past the location of minimum pressure moves the transition at the ideal N_{cr} upstream compared with design M, but this also reduces the sensitivity of Tr_u to N_{cr} at high N_{cr} values. Both effects combine to reduce $C_{d|\sigma}$.

Off-design analysis of the selected optimised aerofoils has also been carried out. Figure 17 shows $C_{d|\mu}$ and $C_{d|\sigma}$ for the NLF0215 and selected optimised designs at a range of lift coefficients. The analysis carried out previously showed that the standard deviation of the transition location, and thus drag, is smallest when the sensitivity of the transition location to the lift coefficient at the ideal N_{cr} is low. As the selected optimised designs have a reduced $C_{d|\sigma}$ at the design lift coefficient, the sensitivity of $C_{d|\mu}$ to the lift coefficient at the design lift coefficient is also low. By reducing both $C_{d|\sigma}$ and $C_{d|\mu}$, a reduction in $C_{d|\mu}$ is achieved between $C_l = 0.65$ and 1.0 using only a single lift coefficient design point. However, both designs do now feature strong drag bucket shapes and higher mean drag than the NLF0215 above $C_l = 1.0$. $C_{d|\sigma}$ also peaks at the upper end of the $C_{d|\sigma}$ bucket lift coefficient range. The analysis carried out

https://doi.org/10.1017/aer.2020.63 Published online by Cambridge University Press

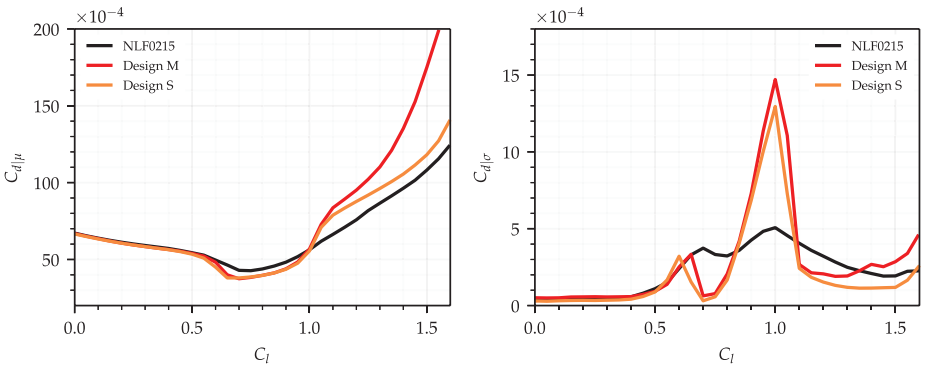


Figure 17. Mean drag and standard deviation of drag polars for the NLF0215 and selected optimised designs.

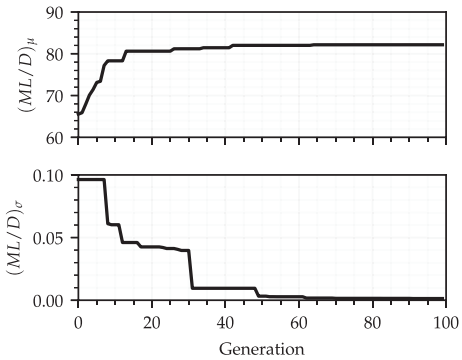


Figure 18. Minimum value found for mean ML/D and standard deviation of ML/D during optimisation.

previously showed that a more rapid movement of the transition location over a smaller lift coefficient range at the ideal N_{cr} resulted in a larger peak in the standard deviation of the transition location, and thus drag. The larger peak in $C_{d|\sigma}$ at $C_l = 1.0$ seen with both optimised designs comes from this larger movement of the transition location over a smaller lift coefficient range. These results indicate that aerofoil designs that are insensitive to changes in N_{cr} and so changes in the lift coefficient on-design become more sensitive off-design to both.

5.2 Transonic results

The optimisation produced 4,800 unique designs before the 100 generations limit. CVGK was able to converge 1,504 of these at all N_{cr} sample points. Figure 18 shows the minimum mean ML/D ($(ML/D)_\mu$) and the standard deviation of ML/D ($(ML/D)_\sigma$) found during the optimisation. Neither objectives improve after 70 iterations, which suggests an optimum of each is found. The Pareto front found between the objects is shown in Fig. 19. All Pareto-front designs have a lower $(ML/D)_\sigma$ than the RAE2822, but some designs only achieve this with a smaller $(ML/D)_\mu$. The maximum $(ML/D)_\mu$ found is much larger than for the RAE2822. A reduction in $(ML/D)_\sigma$ can be obtained by allowing a small decrease in $(ML/D)_\mu$, but reducing $(ML/D)_\sigma$ further then results in a substantial drop in $(ML/D)_\mu$. The optimised designs with maximum $(ML/D)_\mu$, minimum $(ML/D)_\sigma$ and an aerofoil trading off between the two variables

https://doi.org/10.1017/aer.2020.63 Published online by Cambridge University Press

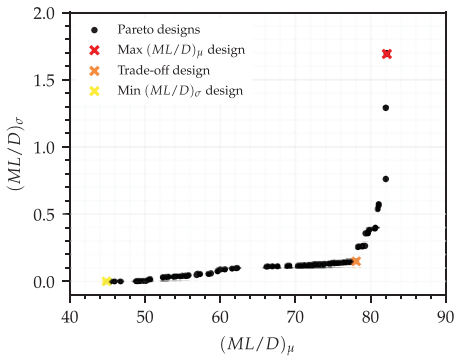


Figure 19. Mean ML/D and standard deviation of ML/D for Pareto-front designs.

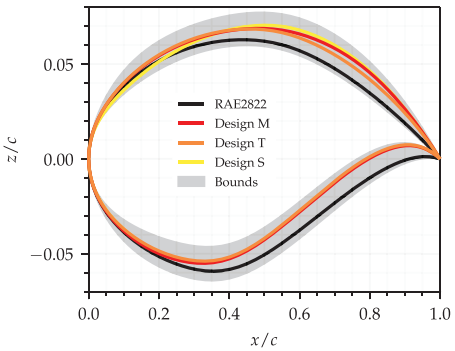


Figure 20. Aerofoil profiles for the RAE2822 and selected optimised designs.

are also highlighted in Fig. 19 and selected for comparison against the RAE2822. These are denoted design M (standing for maximum mean ML/D), design S (standing for minimum standard deviation of ML/D) and design T (standing for a trade-off between the objectives).

Aerofoil profiles for the RAE2822 and selected optimised designs are shown in Fig. 20, with the grey-shaded area indicating the viable design region dictated by the design variable bounds. The optimised aerofoils have an increased camber compared with the RAE2822. The increase is largest at the trailing edge to help lower the angle-of-attack required to obtain the target lift coefficient. The leading-edge curvature is increased for designs M and T but reduced for design S. Figure 21 shows the pressure distributions for the RAE2822 and selected optimised aerofoils at the ideal $N_{cr} = 9$. The reduced angle-of-attack and increased leading-edge curvature result in a long favourable pressure gradient for designs M and T. This extended the laminar flow on the upper surface of both designs by delaying the shock position, while also helping to suppress instability growth. Design M is slightly thicker than design T and so operates at a lower angle-of-attack. As such, it is able to obtain a weaker and more delayed shock. In contrast to this, design S has an increased leading-edge curvature and so sees a strong shock and earlier transition close to the leading edge.

Figure 22 shows how ML/D and Tr_u vary with N_{cr} for the RAE2822 and selected optimised design. All the designs see no change in ML/D until $N_{cr} < 6$, as the low instability amplification means that the upper-surface transition is shock induced. Both designs M and T have a higher ML/D than the RAE2822 over the entire N_{cr} range. Laminar flow has been extended on

https://doi.org/10.1017/aer.2020.63 Published online by Cambridge University Press

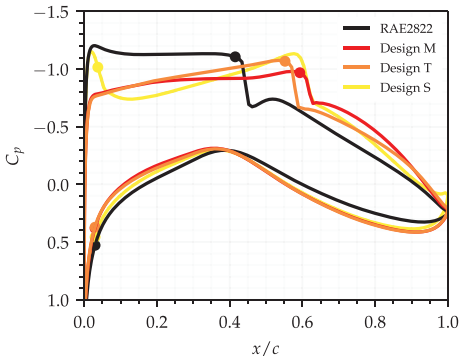


Figure 21. Pressure distributions for the RAE2822 and selected optimised designs.

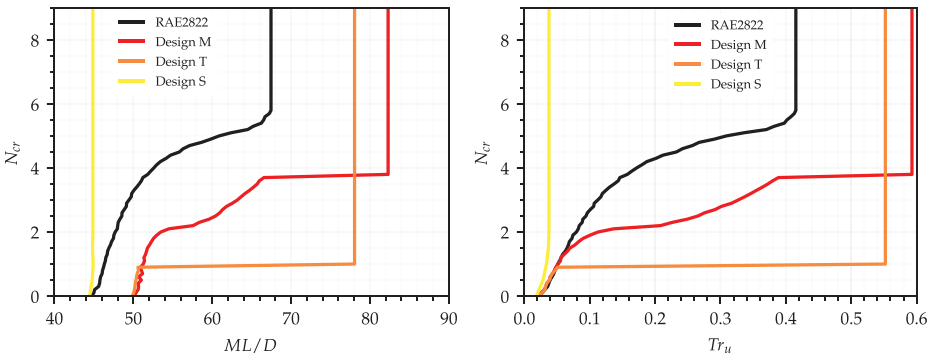


Figure 22. Variation of ML/D and upper-surface transition location with changes in N_{cr} for the RAE2822 and selected optimised aerofoils.

both designs by moving the shock position downstream. Laminar flow is maintained on both designs at lower N_{cr} values due to the stronger favourable pressure gradient obtained. The N_{cr} value where the instability-induced transition first occurs is lower for design T than design M as the favourable pressure gradient obtained is stronger. However, design T has a lower maximum ML/D than design M as this causes a stronger shock positioned further upstream. Fixing the transition near the leading edge at $N_{cr} = 9$ means that design S sees almost no change in ML/D as N_{cr} is reduced. While this design has a very low $(ML/D)_\sigma$, it is of no practical use to a designer given its extremely low $(ML/D)_\mu$. The transition location envelope closely matches the ML/D envelope for all the designs when $N_{cr} > 2$. Designs M and T have higher ML/D below $N_{cr} = 2$, indicating that they perform better than the RAE2822 under turbulent conditions.

Off-design analysis of designs M and T has also been performed for comparison against the RAE2822. Design S was excluded due to its poor $(ML/D)_\mu$ value. Figure 23 shows the $(ML/D)_\mu$ and $(ML/D)_\sigma$ polars for the RAE2822 and selected optimised designs at a range of Mach numbers. Both optimised designs have a larger $(ML/D)_\mu$ and smaller $(ML/D)_\sigma$ than the RAE2822 over the entire Mach number range investigated. Design M has the largest $(ML/D)_\mu$ above the design Mach number. This is due to its having a weaker but longer favourable pressure gradient and so most delayed shock position. The stronger but shorter favourable

https://doi.org/10.1017/aer.2020.63 Published online by Cambridge University Press

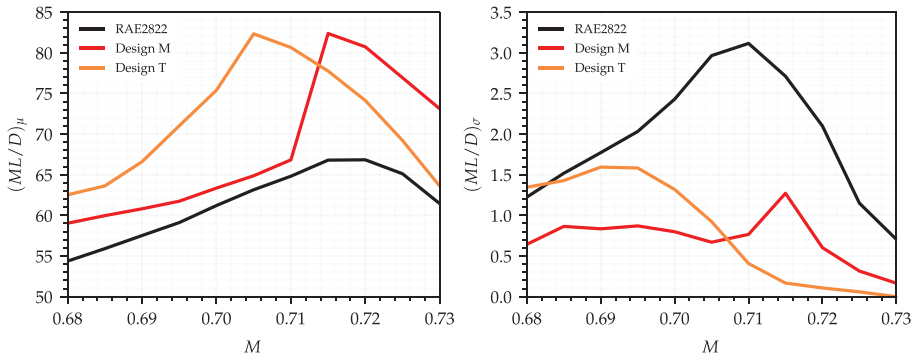


Figure 23. Mean ML/D and standard deviation of ML/D polars for the RAE2822 and selected optimised aerofoils.

pressure gradient of design T results in an earlier shock but better instability suppression at high Mach numbers. Design M sees a large reduction in $(ML/D)_\mu$ below the design Mach number. This is due to a sudden upstream movement of the transition location at the ideal N_{cr} triggered by the laminar boundary-layer solver detecting flow separation in the presence of a strong adverse pressure gradient. As less laminar flow is obtained, design M also sees a reduction in $(ML/D)_\sigma$. As design T features a stronger favourable pressure gradient at the design Mach number, the transition location is slower to move upstream as the Mach number is reduced, and laminar boundary-layer separation is not detected until below $\mathrm{M} = 0.705$. Design T does, however, see an increase in $(ML/D)_\sigma$ as the Mach number is reduced. As $\mathrm{M}^2 C_l$ is fixed, reducing the Mach number increases the lift coefficient and so the angle-of-attack. This results in a less favourable and more adverse pressure gradient that promotes upstream instability growth.

It is important to note that the transition location oscillates substantially during the convergence of cases with laminar separation. A much stronger under-relaxation of the transition location and an increased iteration limit not specified during the optimisation was needed to converge these cases. As such, a uniformly spaced sampling method for uncertainty propagation may not be appropriate when laminar separation is encountered. Furthermore, CVGK is not able to model laminar separation bubbles or re-lamination of the boundary layer, which may be occurring for these cases. These limitations are not, however, felt to affect the validity of the trends observed.

6.0 CONCLUSIONS

The effect of uncertainty in the critical N-factor (N_{cr}) on the performance and shape optimisation of natural laminar flow aerofoils has been investigated. Uncertainty in N_{cr} can be attributed to a degradation in the surface and flow quality, which is not directly modelled but assumed to be crudely incorporated through a reduction in N_{cr}. Uncertainty in N_{cr} is modelled using a negative half-normal probability distribution.

Analysis of the NLF0215 aerofoil showed that the standard deviation of the transition location caused by uncertainty in N_{cr} is largest when the transition location at the ideal N_{cr} is sensitive to changes in the lift coefficient. An estimate of the standard deviation of the transition location with uncertainty in N_{cr} can therefore be made using the aerofoil's transition location polar at the ideal N_{cr}. This is beneficial as it allows for an initial prediction of the most

https://doi.org/10.1017/aer.2020.63 Published online by Cambridge University Press

uncertain transition polar regions without the use of uncertainty analysis methods. The standard deviation of the drag is proportional to the combined standard deviation of the upper- and lower-surface transition locations at low lift coefficient values. This is not so at high lift coefficients, as even small changes in the upper-surface transition location cause large variations in the pressure drag. Analysis of the RAE2822 showed that the standard deviation of ML/D (when M^2C_l is fixed) is proportional to the standard deviation of the upper-surface transition location. The standard deviation of ML/D is largest when ML/D at the ideal N_{cr} is high, and reduces as Mach number is increased and decreased from this point. The transition lies close to the leading edge at low Mach numbers and so is insensitive to N_{cr}. A strong favourable pressure gradient suppresses instability growth up to the downstream shock position at high Mach numbers.

Robust shape optimisation of each aerofoil was then carried out with the goal of reducing the mean drag and the standard deviation of the drag for the NLF0215, and increasing the mean ML/D and reducing the standard deviation of ML/D for the RAE2822. In both cases, the optimiser is able to produce designs that have improved mean performance and a reduced standard deviation of performance with uncertainty in N_{cr} at the design conditions. However, a trade-off is found between the two objectives once they are sufficiently reduced. Off-design analysis of several optimised aerofoils showed that improvements in the mean and standard deviation of the performance on-design can both reduce when off-design.

Because of this, further work on this topic could aim to extend the methodology used to allow for robust optimisation with uncertainty in N_{cr} at a range of Mach numbers or lift coefficients. As the approach used in this study requires a large number of N_{cr} samples per design point, this may be too computationally expensive. Work may need to be done to reduce the computational cost of the optimisation or uncertainty quantification methods to compensate. Any further work should also consider pitching moment, as this increased considerably for the optimised aerofoils generated during this study. These designs will therefore incur a trim drag penalty, which may negate any drag reductions found. Finally, only 2D flow was considered during this study. For transonic aerofoils with wing sweep, three-dimensional cross-flow instabilities become important. As the design requirements for suppression of cross-flow instabilities differ from suppression of Tollmien–Schlichting instabilities, analysis of 3D flows would make for another interesting extension to this work.

ACKNOWLEDGEMENTS

The authors acknowledge financial support from the UK Engineering and Physical Sciences Research Council (EPSRC) and Airbus. The authors would also like to thank James Alderman from Airbus Group Innovations (AGI) for his guidance on aerodynamic design methods used in industry.

REFERENCES

1. THOMAS, A.S.W. Aircraft drag reduction technology - a summary, in *Aircraft Drag Prediction And Reduction*, No. 723, Chapter 1, Advisory Group for Aerospace Research and Development (AGARD), July 1985.
2. WAGNER, R. and FISCHER, M. Developments in the NASA transport aircraft laminar flow program, 21st Aerospace Sciences Meeting, No. AIAA 83-0090, Reno, Navada, USA, January 1983. doi: 10.2514/6.1983-90.

https://doi.org/10.1017/aer.2020.63 Published online by Cambridge University Press

3. VAN DAM, C.P. and HOLMES, B.J. Boundary-layer transition effects on airplane stability and control, *J Aircr*, 1988, **25**, (8), pp 702–709. doi: 10.2514/3.45647.
4. BRASLOW, A.L. and FISCHER, M.C. Design considerations for application of laminar flow control systems, Aircraft Drag Prediction and Reduction, No. 723, Chapter 4, Advisory Group for Aerospace Research and Development (AGARD), July 1985.
5. JOSLIN, R.D. Aircraft laminar flow control, *Annu Rev Fluid Mech*, 1998, **30**, (1), pp 1–29. doi: 10.1146/annurev.fluid.30.1.1.
6. YOUNG, T.M. and HUMPHREYS, B. Liquid anti-contamination systems for hybrid laminar flow control aircraft – a review of the critical issues and important experimental results, *J Aerosp Eng*, 2004, **218**, (4), pp 267–277. doi: 10.1243/0954410041872825.
7. TAGUCHI, G. and WU, Y. *Introduction to Off-Line Quality Control*, Central Japan Quality Control Assoc., 1979.
8. ROBITAILLE, M., MOSAHEBI, A. and LAURENDEAU, É. Design of adaptive transonic laminar airfoils using the $\gamma - \mathrm{Re}_{\theta t}$ transition model, *Aerosp Sci Technol*, 2015, **46**, pp 60–71. doi: 10.1016/j.ast.2015.06.027.
9. RASHAD, R. and ZINGG, D.W. Aerodynamic shape optimization for natural laminar flow using a discrete-adjoint approach, *AIAA J*, 2016, **54**, (11), pp 3321–3337. doi: 10.2514/1.J054940.
10. HUYSE, L. and LEWIS, R.M. Aerodynamic shape optimization of two-dimensional airfoils under uncertain conditions, ICASE Report 2001-1, NASA, Langley Research Center, Hampton, Virginia, USA, January 2001.
11. LI, W., HUYSE, L. and PADULA, S. Robust airfoil optimization to achieve consistent drag reduction over a Mach range, Contractor Report 211042, NASA, Langley Research Center, Hampton, Virginia, USA, August 2001.
12. LI, W. and PADULA, S. Using high resolution design spaces for aerodynamic shape optimization under uncertainty, TP 2004-213003, NASA, Langley Research Center, Hampton, Virginia, USA, March 2004.
13. LEE, D.S., GONZALEZ, L.F., PERIAUX, J. and SRINIVAS, K. Robust design optimisation using multi-objective evolutionary algorithms, *Comput Fluids*, 2008, **37**, pp 565–583. doi: 10.1016/j.compfluid.2007.07.011.
14. SHIMOYAMA, K., OYAMA, A. and FUJII, K. Development of multi-objective six-sigma approach for robust design optimization, *J Aerosp Comput Inf Commun*, 2008, **5**, (8), 215–233. doi: 10.2514/1.30310.
15. XIAOPINGA, Z., JIFENGB, D., WEIJIA, L. and YONG, Z. Robust airfoil optimization with multi-objective estimation of distribution algorithm, *Chin J Aeronaut*, 2008, **21**, pp 289–295. doi: 10.1016/S1000-9361(08)60038-2.
16. CROICU, A.-M., HUSSAINI, M.Y., JAMESON, A. and KLOPFER, G. Robust airfoil optimization using maximum expected value and expected maximum value approaches, *AIAA J*, 2012, **50**, (9), pp 1905–1919. doi: 10.2514/1.J051467.
17. SHAH, H., HOSDER, S., KOZIEL, S., TESFAHUNEGN, Y.A. and LEIFSSON, L. Multi-fidelity robust aerodynamic design optimization under mixed uncertainty, *Aerosp Sci Technol*, 2015, **45**, pp 17–29. doi: 10.1016/j.ast.2015.04.011.
18. COOK, L.W. and JARRETT, J.P. Robust airfoil optimization and the importance of appropriately representing uncertainty, *AIAA J*, 2017, **55**, (11), pp 3925–3939. doi: 10.2514/1.J055459.
19. COOK, L.W., JARRETT, J.P. and WILLCOX, K.E. Extending horsetail matching for optimization under probabilistic, interval, and mixed uncertainties, *AIAA J*, 2018, **56**, (2), pp 849–861. doi: 10.2514/1.J056371.
20. ZHAO, L., DAWES, W.N., PARKS, G., JARRETT, J.P. and YANG, S. Robust airfoil design with respect to boundary layer transition, 50th AIAA/ASME/ASCE/AHS/ASC Structures, Structural Dynamics, and Materials Conference, number AIAA 2009-2273, Palm Springs, California, USA, May 2009. doi: 10.2514/6.2009-2273.
21. ZHAO, K., GAO, Z.-H. and HUANG, J.-T. Robust design of natural laminar flow supercritical airfoil by multi-objective evolution method, *Appl Math Mech*, 2014, **35**, pp 191–202. doi: 10.1007/s10483-014-1783-6.
22. JING, L., ZHENGHONG, G., JIANGTAO, H. and KE, Z. *Chin J Aeronaut*, 2013, **26**, (2), pp 309–318. doi: 10.1016/j.cja.2013.02.007.
23. SALAHUDEEN, A. and BAEDER, J.D. Uncertainty quantification for free stream turbulence intensity effects on airfoil characteristics, AIAA Aerospace Sciences Meeting, No AIAA 2018-0033, Kissimmee, FL, USA, January 2018. doi: 10.2514/6.2018-0033.

https://doi.org/10.1017/aer.2020.63 Published online by Cambridge University Press

24. DENG, L. and QIAO, Z.D. A multi-point inverse design approach of natural laminar flow airfoils, 27th International Congress of the Aeronautical Sciences, Nice, France, September 2010.
25. HAN, Z.-H., CHEN, J., ZHU, Z. and SONG, W.-P. Aerodynamic design of transonic natural-laminar-flow (nlf) wing via surrogate-based global optimization, 54th AIAA Aerospace Sciences Meeting, No. AIAA 2016-2041, San Diago, CA, USA, January 2016. doi: 10.2514/6.2016-2041.
26. DRELA, M. Xfoil: An analysis and design system for low Reynolds number airfoils, in Mueller, T.J. (Ed), *Low Reynolds Number Aerodynamics*, Notre Dame, Indiana, USA, Springer, June 1989, Berlin, Heidelberg, pp 1–12. doi: 10.1007/978-3-642-84010-4_1.
27. DRELA, M. and GILES, M.B. Viscous–inviscid analysis of transonic and low Reynolds number airfoils, *AIAA J*, 1987, **25**, (10), pp 1347–1355.
28. ATKIN, C.J. and GOWREE, E.R. Recent developments to the viscous Garabedian and Korn method, 28th International Congress of the Aeronautical Sciences, Brisbane, Australia, September 2012.
29. LOCK, R.C. and WILLIAMS, B.R. Viscous-inviscid interactions in external aerodynamics, *Prog Aerosp Sci*, 1987, **24**, pp 51–171.
30. GARABEDIAN, P.R. and KORN, D.G. Analysis of transonic airfoils, *Commun Pure Appl Math*, 1971, **24**, (6), pp 841–851.
31. LOCK, R.C. A review of methods for predicting viscous effects on aerofoils and wings at transonic speeds, in *Computation of Viscous–Inviscid Interactions*, No. 291, Chapter 2, Advisory Group for Aerospace Research and Development (AGARD), May 1981.
32. GREEN, J.E., WEEKS, D.J. and BROOMAN, J.W.F. Prediction of turbulent boundary layers and wakes in compressible flow by a lag-entrainment method, Tech Rep 3791, Aeronautical Research Council, Aerodynamics Department, RAE Farnborough, UK, 1977.
33. ATKIN, C.J. Convergence of calculated transition loci during computational analysis of transonic aerofoils and infinite swept wings, 29th Congress of the International Council of the Aeronautical Sciences, St. Petersburg, Russia, September 2014.
34. GOWREE, E.R. *Influence of Attachment Line Flow on Form Drag*, PhD thesis, City University, London, UK, May 2014.
35. SOMERS, D.M. Design and experimental results for a flapped natural-laminar-flow airfoil for general aviation applications, TP 1865, NASA, Langley Research Center, Hampton, Virginia, USA, June 1981.
36. WICKE, K., LINKE, F., GOLLNICK, V. and KRUSE, M. Insect contamination impact on operational and economic effectiveness of natural-laminar-flow aircraft, *J Aircr*, 2016, **53**, (1), pp 158–167. doi: 10.2514/1.C033237.
37. SMITH, A.M.O. and GAMBERONI, N. Transition, Pressure Gradient and Stability Theory, Tech Rep 26388, Douglas Aircraft Company, El Seguno, CA, USA, August 1956.
38. DRELA, M. Design and optimization method for multi-element airfoils, Aerospace Design Conference, No. AIAA 93-0969, Irvine, CA, USA, February 1993. doi: 10.2514/6.1993-969.
39. DRIVER, J. and ZINGG, D.W. Numerical aerodynamic optimization incorporating laminar-turbulent transition prediction, *AIAA J*, 2007, **45**, (8), pp 1810–1818. doi: 10.2514/1.23569.
40. COOK, P.H., MCDONALD, M.A. and FIRMIN, M.C.P. Aerofoil RAE 2822 - pressure distributions, and boundary layer and wake measurements, Experimental Data Base for Computer Program Assessment, No. 138, Advisory Report A6, Advisory Group for Aerospace Research and Development (AGARD), May 1979.
41. TAMIGNIAUX, T.L.B., STARK, S.E. and BRUNE, G.W. An experimental investigation of the insect shielding effectiveness of a Krueger flap/wing airfoil configuration, 5th Applied Aerodynamics Conference, No 87-2615, Monterey, CA, USA, August 1987, AIAA. doi: 10.2514/6.1987-2615.
42. BOEING CO. High Reynolds number hybrid laminar flow control (HLFC) flight experiment II. Aerodynamic design, Tech Rep CR-1999-209324, NASA, Langley Research Center, Hampton, Virginia, USA, April 1999.
43. VAN DAM, C.P. The aerodynamic design of multi-element high-lift systems for transport airplanes, *Prog Aerosp Sci*, 2002, **38**, (2), pp 101–144. doi: 10.1016/S0376-0421(02)00002-7.
44. SCHRAUF, G. Large-scale laminar flow tests evaluated with linear stability theory, 19th Applied Aerodynamics Conference, AIAA, June 2001.
45. SCHMITT, V., ARCHAMBAUD, J.P., HORSTMANN, K.H. and QUAST, A. Hybrid laminar fin investigations, Active Control Technology for Enhanced Performance Operational Capabilities of Military Aircraft, Land Vehicles and Sea Vehicles, No RTO-MP-051, Braunschweig, Germany, June 2001. doi: 10.14339/RTO-MP-051.

https://doi.org/10.1017/aer.2020.63 Published online by Cambridge University Press

46. FORTIN, F.-A., RAINVILLE, F-M.D., GARDNER, M.-A., PARIZEAU, M. and GAGNÉ, C. Deap: Evolutionary algorithms made easy, *J Mach Learn Res*, 2012, **13**, pp 2171–2175.
47. DEB, K., PRATAP, A., AGARWAL, S. and MEYARIVAN, T. A fast and elitist multiobjective genetic algorithm: NSGA-II, *IEEE Trans Evol Comput*, 2002, **6**, (2), pp 182–197. doi: 10.1109/4235.996017.
48. DEB, K. and AGRAWAL, R.B. Simulated binary crossover for continuous search space, *Complex Syst*, 1995, **9**, (9), pp 115–148.
49. DEB, K. and AGRAWAL, S. A niched-penalty approach for constraint handling in genetic algorithms, Artificial Neural Nets and Genetic Algorithms, Slovenia, Indian Institute of Technology Kanpur, Springer, 1999, pp 235–243.
50. MASTERS, D.A., TAYLOR, N.J., RENDALL, T.C.S., ALLEN, C.B. and POOLE, D.J. Review of aerofoil parameterisation methods for aerodynamic shape optimisation, 53rd AIAA Aerospace Sciences Meeting and Exhibit, No AIAA 10.2514/6.2015-0761, Kissimmee, FL, USA, January 2015. doi: 10.2514/6.2015-0761.
51. ALANDER, J.T. On optimal population size of genetic algorithms, Computer Systems and *Software Engineering* 1992, The Hague, Netherlands, IEEE, May 1992, pp 65–70. doi: 10.1109/CMPEUR.1992.218485.
52. STORN, R. On the usage of differential evolution for function optimization, North American Fuzzy Information Processing, Berkeley, California, USA, IEEE, June 1996, pp 519–523.
53. KULFAN, B.M. Universal parametric geometry representation method, *J Aircr*, 2008, **45**, (1), pp 142–158. doi: 10.2514/1.29958.

https://doi.org/10.1017/aer.2020.63 Published online by Cambridge University Press